





# Pervasive fire danger continued under a negative emission scenario

Received: 22 February 2024

Accepted: 6 November 2024

Published online: 19 November 2024

Hyo-Jeong Kim <sup>1,2,3</sup>, Jin-Soo Kim <sup>1,2</sup> , Soon-Il An <sup>3</sup> , Jongsoo Shin <sup>4</sup>, Ji-Hoon Oh <sup>5</sup> & Jong-Seong Kug <sup>5</sup>

Enhanced fire-prone weather under greenhouse gas warming can significantly affect local and global carbon budgets from increased fire occurrence, influencing carbon-climate feedbacks. However, the extent to which changes in fire-prone weather and associated carbon emissions can be mitigated by negative emissions remains uncertain. Here, we analyze fire weather responses in CO<sub>2</sub> removal climate model experiments and estimate their potential carbon emissions based on an observational relationship between fire weather and fire-induced CO<sub>2</sub> emissions. The results highlight that enhanced fire danger under global warming cannot be restored instantaneously by CO<sub>2</sub> reduction, mainly due to atmospheric dryness maintained by climatic inertia. The exacerbated fire danger is projected to contribute to extra CO<sub>2</sub> emissions in 68% of global regions due to the hysteresis of climate responses to CO<sub>2</sub> levels. These findings highlight that even under global cooling from negative emissions, increased fire activity may reinforce the fire-carbon-climate feedback loop and result in further socio-economic damage.

Devastating fire occurrences worldwide have garnered the growing attention of the academic community and the public. These wildfires inflict not only instantaneous socio-economic damages<sup>1–4</sup> but also have long-lasting impacts on the Earth system by providing carbon dioxide (CO<sub>2</sub>) and aerosols to the atmosphere, altering landscape compositions, and disturbing the ecosystem<sup>5–11</sup>. One of the most critical impacts on shaping our future is the significant amount of CO<sub>2</sub> released into the atmosphere, leading to the positive feedback that amplifies global warming<sup>12,13</sup>. The annual total of fire carbon emissions (C<sub>Fire</sub>) is estimated to be 21–36% of man-made emissions (2000–2020)<sup>14</sup>, with an average of ~2 PgC per year (1 PgC = 10<sup>15</sup> g of carbon; Fig. 1a, asterisks). Being such a major carbon emitter, the trend towards more frequent large fires<sup>15–17</sup> raises concerns about further climate change in the future.

An accurate future fire prediction is crucial but challenging<sup>18</sup> due to the complexity of fire dynamics related to multiple factors such as fuel availability, ignition agents, human control, and weather

conditions. Nevertheless, weather conditions are generally considered critical factors in shaping recent<sup>17,19–21</sup> and future<sup>18,22–27</sup> fire trends. Indeed, there is a broad consensus that anthropogenic climate change toward warmer and drier conditions will exacerbate fire danger. However, estimations for future carbon emissions from increased fires are still uncertain<sup>13,28,29</sup>.

Meanwhile, recent studies have reported that the climate system exhibits hysteresis with respect to the reduced CO<sub>2</sub> forcing<sup>30,31</sup>. That is, the climate state is not immediately recovered even if the CO<sub>2</sub> concentration is returned to the previous level—for instance, the global surface temperature still remains high due to the large thermal inertia of the ocean, the recovery of the weakened thermohaline circulation (THC) is delayed<sup>32</sup>, and the latitudinal position of the Intertropical Convergence Zone (ITCZ) stays at south compared to its original position<sup>31</sup>. The associated changes in surface weather are not experienced homogeneously across regions and/or variables (e.g., refs. 30,33.). However, its influence on fire danger remains

<sup>1</sup>School of Energy and Environment, City University of Hong Kong, Hong Kong, China. <sup>2</sup>Center for Ocean Research in Hong Kong and Macao (CORE), The Hong Kong University of Science and Technology, Hong Kong, China. <sup>3</sup>Department of Atmospheric Sciences/Irreversible Climate Change Research Center, Yonsei University, Seoul, South Korea. <sup>4</sup>Woods Hole Oceanographic Institution, Woods Hole, MA, USA. <sup>5</sup>School of Earth and Environmental Sciences, Seoul National University, Seoul, South Korea. ✉ e-mail: [jinsoo.kim@cityu.edu.hk](mailto:jinsoo.kim@cityu.edu.hk); [sian@yonsei.ac.kr](mailto:sian@yonsei.ac.kr)

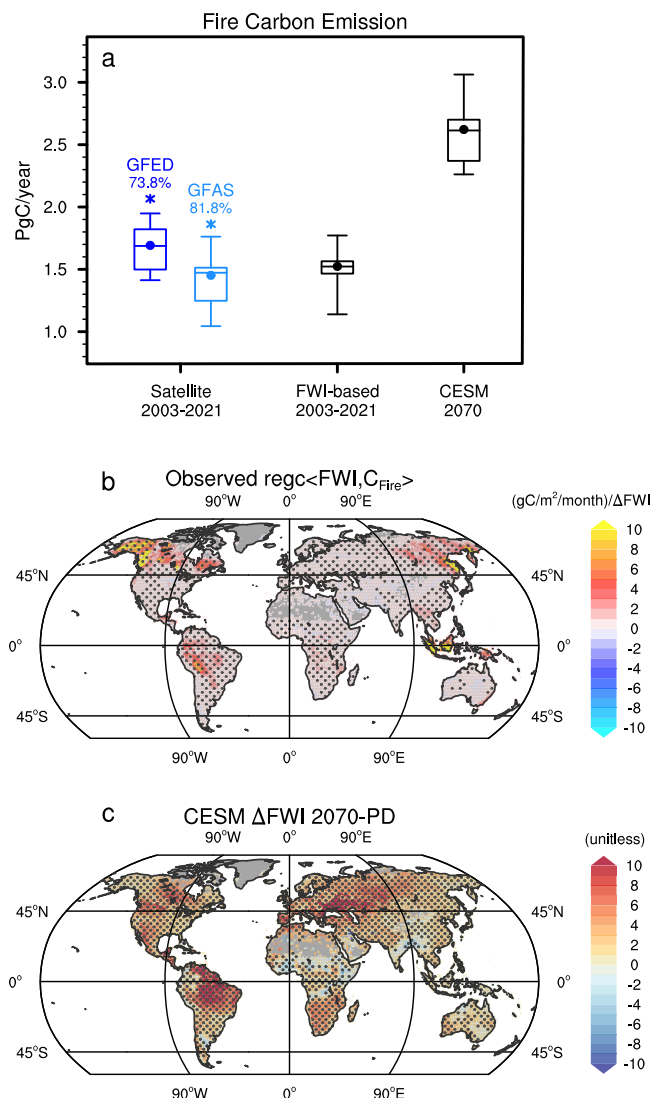


**Fig. 1 | Fire weather and fire emissions from the satellite and doubling  $\text{CO}_2$  simulation. a** Box plots showing distributions of fire season  $C_{\text{Fire}}$  for the satellite products (dark and light blue), estimated  $C_{\text{Fire}}$  using ERA5-derived fire weather index (FWI; black, middle), and estimated  $C_{\text{Fire}}$  in 2070 using model-simulated FWI (black, right). Each horizontal break indicates the minimum, 25% quantile, median, 75% quantile, and maximum, from bottom to top. For CESM results, each break represents the average of 28 ensembles. Dots indicate the mean. The relative portion of fire season emissions to the annual total (asterisks) is marked by numbers (%) for the observation. **b** Regression coefficients between ERA5 FWI (unitless) and GFED  $C_{\text{Fire}}$  ( $\text{g m}^{-2} \text{ month}^{-1}$ ) during 1998–2021; only the months within the fire season (3 months  $\times$  24 years = 72 months) were considered. **c** Differences in FWI between the average of 11 years centered at 2070 (2065–2075) and baseline period (Present Day; PD) in CESM. The ensemble average is shown ( $N = 28$ ). In b and c, dots indicate statistically significant values at the 95% confidence level from a two-tailed  $t$ -test.

unexplored, causing uncertainty about how fire weather will respond to global cooling under carbon reduction policies.

Minimizing these uncertainties will allow more accurate climate predictions and the prioritization of effective mitigation and adaptation strategies. Understanding the internal feedback processes within the climate system, specifically isolating the effects of climate change from non-climatic factors, will greatly benefit achieving these goals. Therefore, this study investigates global and regional responses of fire weather to an idealized  $\text{CO}_2$  removal scenario using climate model simulations. Also, a quantitative assessment of the potential carbon

release from increased fires is conducted at global and country levels. Our findings demonstrate that fire danger persists even after  $\text{CO}_2$  reduction due mainly to the thermal inertia of the climate system, which in turn can accumulate a significant amount of carbon in the atmosphere. The global trend of prolonged fire danger is regionally modulated by atmospheric and oceanic circulations and this information would support the national greenhouse gas (GHG) inventory management.

## Results

### Observed fire weather–fire emission relationship

The fire behaviors exhibit a clear seasonality under the strong influence of the weather. For example,  $C_{\text{Fire}}$  during fire seasons accounts for 73.8% of the year-round emissions in Global Fire Emissions Database (GFED) v4.1s<sup>34–36</sup> (Fig. 1a), when fire seasons were defined as 3 months centered at the month with the largest  $C_{\text{Fire}}$  (Methods). The year-to-year variabilities between fire season and annual total emissions are closely related ( $r = 0.98$ ), indicating that the fire activity throughout the year highly depends on the fire season. It is also qualitatively similar when using  $C_{\text{Fire}}$  of an independent satellite product [Global Fire Assimilation System (GFAS)]<sup>37</sup>. Therefore, our analysis focuses only on the fire season: variables representing the fire season in any year are hereafter referred to as ‘annual.’

We chose the Canadian fire weather index (FWI) system<sup>38</sup> to diagnose fire risk from daily meteorological variables: 24-h precipitation, near-surface temperature ( $T$ ), relative humidity (RH), and wind speed are used (see “Methods”). With the annual FWI derived from ERA5<sup>39</sup> and  $C_{\text{Fire}}$  from GFED, we constructed a grid-wise regression model that predicts  $C_{\text{Fire}}$  from FWI (Fig. 1b). Both FWI and  $C_{\text{Fire}}$  were preceded by horizontal smoothing within neighboring grids to alleviate the high locality of fire<sup>22,40</sup> (Methods). The regression model indicates a statistically significant positive relationship between FWI and  $C_{\text{Fire}}$  in ~71% of the total ‘fire-prone’ land area (here, ‘fire-prone’ area is defined based on the grid points where fire occurrence has been observed at least once between 1998–2021. See “Methods” for more details). As a previous study pointed out the rising trend of FWI under climate change<sup>17</sup>, the widespread positive relationship between FWI and  $C_{\text{Fire}}$  suggests that fires will be a more substantial modulator of the global carbon budget.

When estimating the C emission from FWI using the regression model, it reproduced a similar range of annual variation ( $0.63 \text{ Pg year}^{-1}$ ) to that of GFED  $C_{\text{Fire}}$  ( $0.54 \text{ Pg year}^{-1}$ ) over the overlapping period for all datasets (2003–2021, Fig. 1a). However, the 1<sup>st</sup>-to-3<sup>rd</sup> quantile distribution is much narrower, and the mean ( $1.52 \text{ Pg year}^{-1}$ ) is underestimated by about 10% compared to GFED ( $1.69 \text{ Pg year}^{-1}$ ). We note that qualitative features are similar even if we only use fire-prone grids where the FWI– $C_{\text{Fire}}$  relationship is significant at the 95% confidence level (two-tailed  $t$ -test, Supplementary Fig. 1). The discrepancy between the GFED and FWI-based estimation reflects some nonlinearities in the FWI– $C_{\text{Fire}}$  relationship that could be inherent or due to the limitation of not considering non-weather control on fire activity. Nevertheless, the mean and spread of FWI-based  $C_{\text{Fire}}$  lie well within the range of two satellite products, indicating its ability to capture the global  $C_{\text{Fire}}$  behavior. Therefore, valuable insights into the carbon–climate cycle feedback can be obtained by applying this regression model to future climate projections, of which, to the best of our knowledge, this study will be the first attempt.

In addition to the global perspective, it is also worth discussing the regional differences in sensitivity (Fig. 1b). High sensitivities are pronounced mainly in the Canadian and Russian boreal forests, the Amazon area, and Southeast Asia, especially for Indonesia. These correspond to the areas where fire activities (e.g., represented by burnt area) are more susceptible to weather conditions due to the “flammability-limited” fire regime: In this regime, atmospheric moisture deficit mainly controls fire activities, contrarily to the “fuel-limited” regime

where fuel availability dominates (e.g., semi-arid areas in Australia or African savannah<sup>22,41,42</sup>). At the same time, they broadly overlap with the global distribution of peatlands, which store a massive amount of carbon at high densities<sup>43,44</sup>. In short,  $C_{\text{Fire}}$  is sensitive to FWI change if the region is in the weather-susceptible fire regime and/or has a carbon-abundant soil component.

### Fire Danger in a Warming Climate

Land surface warming and the subsequent vapor pressure deficit [via the Clausius–Clapeyron (C–C) equation] generally enhance fire risk<sup>17,19–21</sup>. The results from climate model (CESM v1.2<sup>45</sup>, Methods) simulations also depict increased fire danger worldwide under doubled  $\text{CO}_2$  ( $2 \times \text{CO}_2$ ), based on the ensemble mean of 11-year averaged (2065–2075, hereafter ‘2070’) anomalies against the present-day run (PD, the control run representing the 2000 condition) (Fig. 1c). Most (85%) global fire-prone areas undergo enhanced fire risk, yielding a global mean  $\Delta\text{FWI}$  of 2.58 in 2070, which is 15.51% increase compared to PD. Fire hazards are particularly exacerbated in tropical South America, north of the Black Sea, and North America. This is of concern as these regions coincide with key ecosystem regions (e.g., tropical rainforests and boreal forests) and relatively densely populated regions (e.g., Eastern Europe and Western North America).

Another concern from the high fire risk is the surge in carbon emissions. The global increase in FWI in 2070 implies an additional carbon flux ( $\Delta C_{\text{Fire}}$ ) of  $0.92 \text{ PgC year}^{-1}$  from fire season when estimated using the regression model. To assess the total annual flux in 2070, we added the simulated increment to the observed mean ( $1.69 \text{ PgC year}^{-1}$  of GFED): That is, a delta change ( $\Delta$ ) method<sup>46</sup> was applied to calibrate the inherent model bias against the true (observed) mean state (Supplementary Fig. 2). The result of the total  $2.61 \text{ PgC year}^{-1}$  (Fig. 1a), equivalent to a 53% increase in annual  $C_{\text{Fire}}$ , indicates that the contribution of fires to the carbon cycle will be much more substantial and exacerbate climate change. The range of  $C_{\text{Fire}}$  in 2070 inferred from the CESM simulations exceeds those of satellite-observed  $C_{\text{Fire}}$ . It means that the anthropogenic doubling of  $\text{CO}_2$  will likely result in a much higher level of annual  $C_{\text{Fire}}$  that has not been experienced in the satellite-observed era.

### Prolonged Fire Danger under Global Cooling

While the heightened fire danger under greenhouse warming has been widely discussed in the literature (e.g., refs. 17,18,22,23.), the consequences of global cooling under  $\text{CO}_2$  reduction on fire weather have not yet been examined. The results from symmetrical  $\text{CO}_2$  removal experiments (black solid line in Fig. 2a) suggest that fire weather will experience hysteresis: The time evolution of FWI depends on not only the transient value of  $\text{CO}_2$  forcing but also the path that the forcing has gone through. For example, the global mean  $\Delta\text{FWI}$  is 2.58 when the forcing rises to  $2 \times \text{CO}_2$ . However, when the forcing returns to  $2 \times \text{CO}_2$  after the peak (2205–2215, hereafter ‘2210’),  $\Delta\text{FWI}$  has not been fully restored, still amounting to 3.12 (statistically distinguished from that of 2070). The prolonged fire danger continues even after the forcing reaches the initial level and flattens from 2280 onwards. Such a delayed recovery of elevated fire weather can also be found in other climate models, which were subjected to a similar symmetric  $\text{CO}_2$  forcing but with a different initial condition, as part of the Carbon Dioxide Removal Intercomparison Project (CDRMIP; Supplementary Fig. 3). It indicates that even if global efforts towards carbon reduction are successful, dangerous fire weather could be irreversible for a while.

However, such asymmetric response of FWI to  $\text{CO}_2$  is not uniformly experienced globally. Fig. 2b shows residuals of FWI between  $2 \times \text{CO}_2$  periods (2210 minus 2070). One notable feature is a meridional contrast between the two hemispheres. Most fire-prone areas in the Northern Hemisphere (NH, 81%) experience heightened fire danger, while the Southern Hemisphere (SH, 61%) tends to experience diminished fire danger. This feature is more pronounced in the tropics. For

example, at the north of the equator, the more prolonged and enhanced fire danger is featured by positive anomalies in FWI in Central America, North Africa, and South Asia. Contrarily, at the south of the equator, fire danger is rapidly alleviated as  $\text{CO}_2$  decreases, resulting in negative residuals of  $\Delta\text{FWI}$  in South America, Central Africa, and Western Australia. As a result, a contrast centered around the equator is established.

The spatial distribution of hysteresis responses of FWI (2210 minus 2070, Fig. 2b) is quite distinct from that of initial warming responses (2070 minus PD, Fig. 1c). It is also evident when the two responses are directly compared in each region (Fig. 2c). For instance, in some regions, the initial increase in fire danger is followed by further intensification until the  $\text{CO}_2$  return. This is the most pervasive response in Africa, Asia, and Europe. From a global perspective, 58.9% of the fire-prone area belongs to this case. For 15.9%, the increase in fire danger due to the asymmetric response even exceeds that due to the initial warming, making fire risk in 2210 more than doubled compared to the baseline. These areas include parts of Asia, Africa, and America, suggesting they could be more burdened with fire manageability than others. In the European region, the magnitude of the initial response tends to be proportional to that of the asymmetric response: in the region where the fire risk has increased rapidly with  $\text{CO}_2$ , future recovery is likely to be more difficult. For other parts of the globe, such as South America and Australia, global  $\text{CO}_2$  removal can efficiently reduce the already-increased fire risk to a lower level than their previous state. However,  $\text{CO}_2$  removal could have the opposite effect of intensifying fire risk previously weakened in parts of Asia and Africa, albeit in a relatively small area (9.19%). The areas that can be deemed comparatively safe from fire hazards throughout the experiment, where initial and asymmetric responses are both negative, account for only a small fraction (5.18%) of the land area.

### Meteorological driver of hysteresis in fire weather change

To understand the physical processes of the global fire weather evolution, changes in the meteorological variables (namely, global means of 24-h precipitation and near-surface T, wind speed, and RH) and their contributions to  $\Delta\text{FWI}$  were examined (Figs. 2a and 3a). Note that the global means only include fire-prone grids, where fire season can be defined. Notably, the time evolution of T and RH highly resembles that of FWI, rising during  $\text{CO}_2$  ramp-up followed by delayed recovery during  $\text{CO}_2$  ramp-down. The slow recovery of T is mainly attributable to the large inertia of the ocean<sup>32</sup>, with RH being subordinate to it through the C–C relation. Meanwhile, the time evolution of wind speed and precipitation is noisy, characterized by pronounced high-frequency fluctuations and a substantial spread between ensemble members. These features strongly suggest T and RH as the principal drivers of global FWI change in the future, which aligns with previous studies<sup>20,23,47</sup>.

To quantify the contribution from each meteorological variable on  $\Delta\text{FWI}$ , their globally-averaged residuals between  $2 \times \text{CO}_2$  periods (i.e., 2210 minus 2070) were obtained from 28 ensemble simulations, and then a multiple linear regression model was established at each grid point (see ‘Methods’). This method identifies the sensitivity of predictand (in this case,  $\Delta\text{FWI}$ ) to each of multiple predictors (changes in meteorological variables) separately. The contribution from  $i$ -th weather variable to  $\Delta\text{FWI}$  was assessed as the multiplication of the partial regression coefficient ( $\gamma_i$ ) and the change in the variable ( $\Delta_i$ ), that is,  $\gamma_i \times \Delta_i$ <sup>48</sup>. The results show a dominant influence of RH, contributing 110.6% in shaping the FWI hysteresis in a global mean perspective (Fig. 3a) as well as at the regional scale (Supplementary Fig. 5). A qualitative agreement also exists in the spatial distribution of  $\Delta\text{FWI}$  and  $\Delta\text{RH}$  (Figs. 2b and 3b), where negative  $\Delta\text{RH}$  generally overlaps positive  $\Delta\text{FWI}$  and vice versa. Therefore, it is concluded that changes in RH, the atmospheric dryness, predominantly determine the asymmetric response of fire weather to the symmetric  $\text{CO}_2$  forcings.

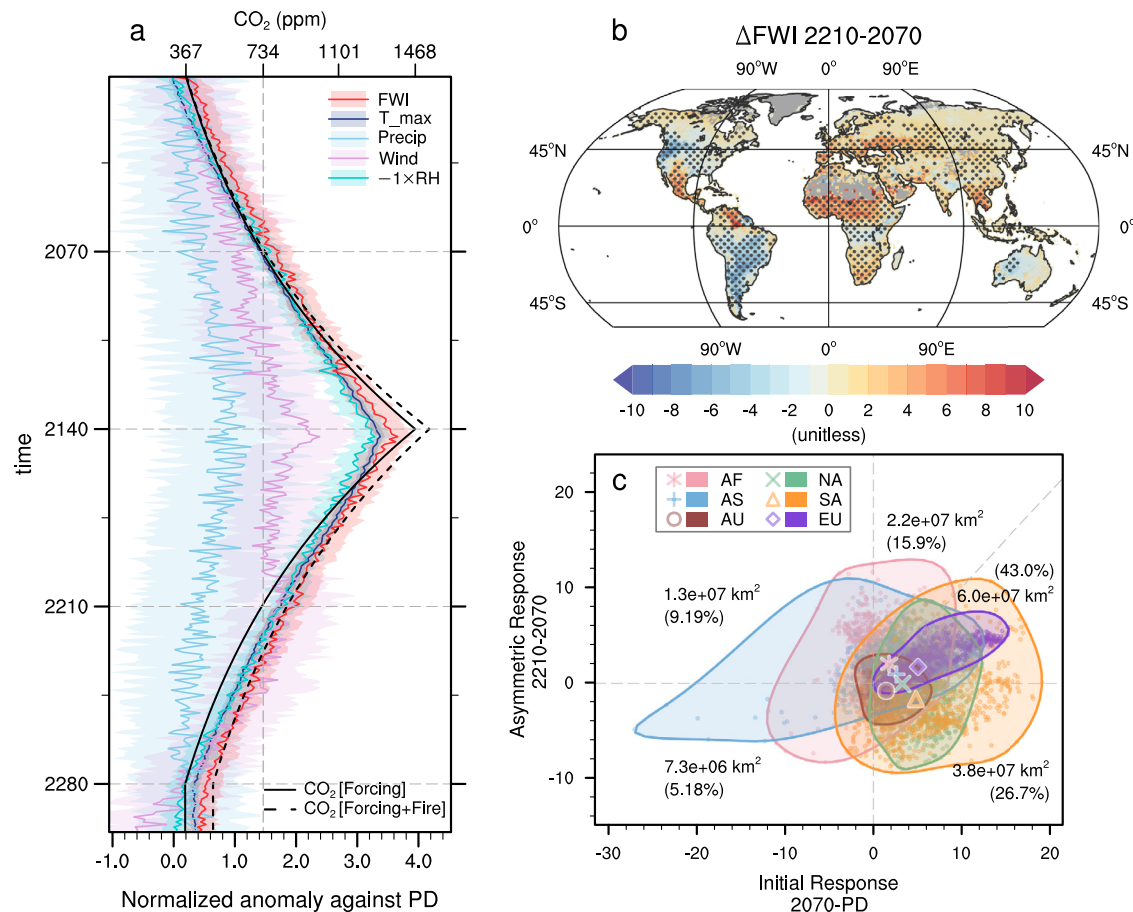


**Fig. 2 | Asymmetric fire weather response to CO<sub>2</sub> forcing.** **a** Time evolutions of the prescribed CO<sub>2</sub> forcing (black solid), fire weather index (FWI; red), and four meteorological variables relevant to FWI (bluish). Relative humidity (RH) was reversed by multiplying -1 to represent dryness. Except for CO<sub>2</sub> forcing, all variables represent global and fire season average values and were standardized by their respective standard deviations. They are presented as the deviation from the control period (Present Day; PD) for visual clarity. Solid lines and shadings represent the ensemble average and one sigma spread, respectively. The black dashed line indicates the sum of prescribed and estimated fire emission forcing (see text),

for which only the ensemble mean is shown. **b** Ensemble mean differences in FWI between '2070' and '2210'. Dots indicate significant changes at the 95% confidence level. **c** Convex polygons for each continent envelop the scatterplots of ΔFWI responses to the initial warming (2070 minus PD) vs reversed (2210 minus 2070) CO<sub>2</sub>. The dashed diagonal in the 1st quadrant represents a 1:1 line. AF: Africa. AS: Asia. AU: Australia. NA: North America. SA: South America. EU: Europe. Numbers represent the area belonging to each section surrounded by the gray dashed line, with the percentage relative to the global total fire-prone areas.

Over the land area, changes in RH can be driven by changes in temperature, which modulate the atmospheric vapor capacity<sup>49</sup>. For example, warming increases the saturation vapor pressure and decreases RH according to the C-C relation. Interestingly, however, RH decreased in some regions despite surface cooling. For instance, in the high-latitude Eurasia region (Fig. 3b), although temperature changes indicate heightened humidity (Fig. 3c and Methods), the simulated ΔRH is negative. This demonstrates that rather than simply the saturation capacity, moisture amount itself significantly decreases, and the final ΔRH is governed by it (Fig. 3b, d). While both local (e.g., reduced evapotranspiration) and non-local (e.g., less moisture transport from the ocean) processes could have contributed to such change, we focus on the role of the latter, given the limited moisture source over the land surface<sup>49</sup>. The negative ΔRH seen in the Eurasian region is due to a reduction in the moisture supply from the North Atlantic (Fig. 3d), which is attributed to the delayed recovery of the THC against the CO<sub>2</sub> forcing. The weakened THC can induce surface cooling over the North Atlantic, substantially suppressing evaporation over the ocean surface<sup>32</sup>. Counter-intuitive RH changes to given temperature changes are also found in the South American south-of-equator region and Australia, indicating moisture gain (Figs. 3b, c). These can be linked to the southward shift of ITCZ during CO<sub>2</sub> ramp-down, which leads to the extra moisture supply to the regions where its

rising branch resides<sup>31</sup>. It is important to note that this delayed recovery in large-scale climate phenomena is likely not model-dependent, as it is commonly observed across different climate models in CDRMIP<sup>31,50</sup>. In summary, moisture redistribution over the land by the lagged recovery of oceanic and atmospheric circulations behind that of CO<sub>2</sub> concentration results in the inhomogeneous spatial pattern of the hysteresis response to fire danger.

## Discussions

It is important to note that our estimate of C<sub>Fire</sub> is based solely on meteorological conditions, excluding feedback from C<sub>Fire</sub> to climate as well as potential future changes in vegetation, ignition sources, or fire management strategies. While this approach was designed to isolate the climatic effect, it is considered an inherent limitation when viewed from the perspective of future predictions. Notably, however, a recent study<sup>28</sup> that considered climate–fire interaction and socioeconomic factors, such as population density, gross domestic product, land use, and land cover change, using Earth system models suggested that annual carbon flux around 2070 under the Shared Socioeconomic Pathways 5–8.5 (SSP5-8.5) scenario could be about 2.8 PgC year<sup>-1</sup> (Fig. 3A of ref. 28.), which was close to the upper end of our estimated range (Fig. 1a); the applied CO<sub>2</sub> concentration in 2070 is ~744 ppm in the SSP5-8.5 scenario<sup>51</sup> and 736 ppm in this study. This consistency



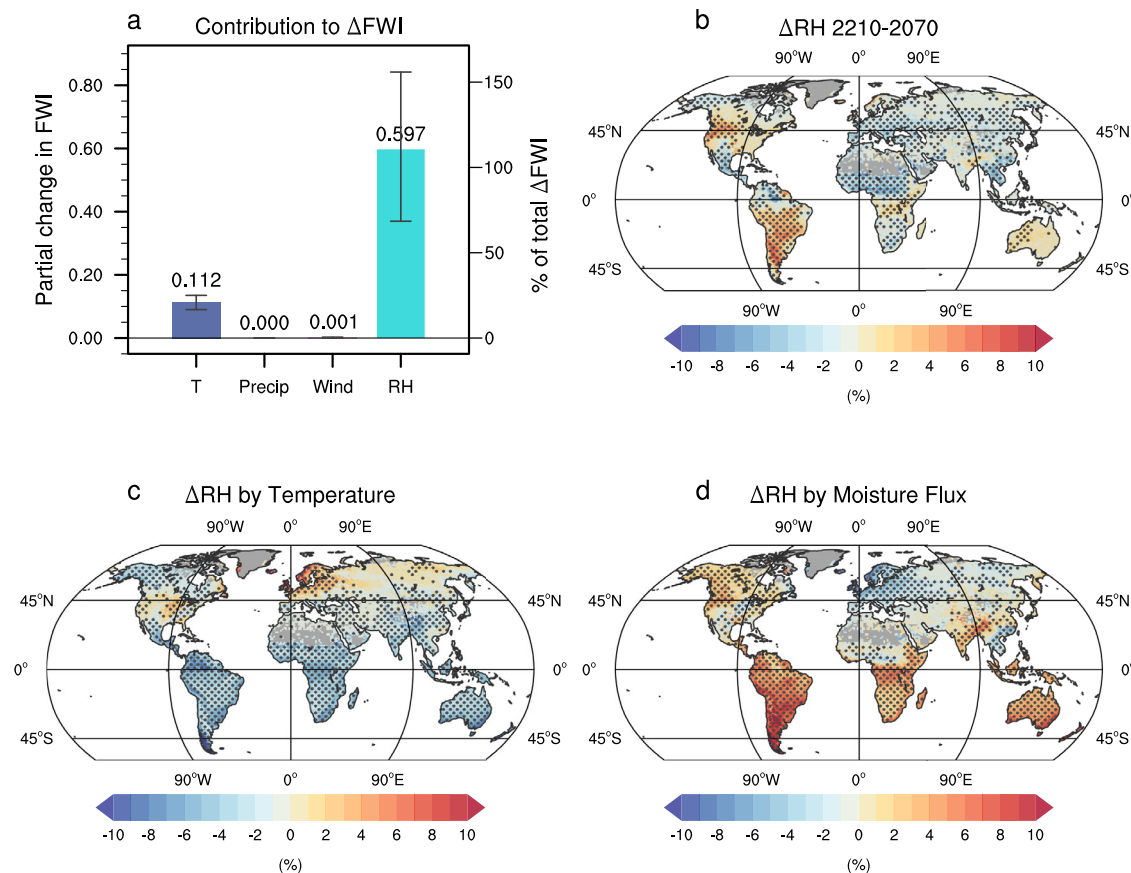


**Fig. 3 | Meteorological driver of irreversible fire weather change. a** Contribution from each weather variable to the global fire weather index (FWI) change, obtained from multiple regression analysis (see “Methods” and Supplementary Fig. 4). Bars indicate 95% confidence intervals from bootstrap sampling ( $N = 1000$ )

**b–d** Ensemble mean differences in relative humidity (RH) between ‘2070’ and ‘2210’. Dots indicate significant changes at the 95% confidence level. **b** The total change, **c** partial change inferred from temperature, and **(d)** the rest, by moisture supply/loss (see “Methods”).

implies that our method captures the essential aspect of fire behavior under changing climate while factors like seasonality (annual vs. fire season only) and assumption of linearity between FWI and  $C_{\text{Fire}}$  (this study) could have affected their discrepancies. It is also suggested that non-weather effects on fire emissions might cancel each other out to some extent, leaving the overall trend largely driven by climate.

Keeping these in mind, we now discuss implications for the national mitigation plan by investigating our FWI-based  $C_{\text{Fire}}$  estimation at the country level. In particular, emissions in response to the symmetric  $\text{CO}_2$  forcing and to  $\text{CO}_2$  halving were compared to the current fire carbon emission, which is defined as the mean value between 1998–2021 (Fig. 4). Russia and Indonesia, which have relatively high fire emissions in the present climate, were the two countries with the largest asymmetric response in  $\Delta C_{\text{Fire}}$  under the symmetric  $\text{CO}_2$  forcing. This was followed by countries in northern Equatorial America, China, and countries on the Indochina Peninsula, which are generally located in the regions with a high FWI– $C_{\text{Fire}}$  sensitivity (Fig. 1b) and/or a large asymmetric change in fire weather (Fig. 2b). The magnitude of  $\Delta C_{\text{Fire}}$  is generally substantial compared to the current  $C_{\text{Fire}}$ , amounting to 13.1% (Indonesia) to 53.9% (Venezuela). This implies that prolonged fire danger could significantly alter the relative importance of their GHG inventory components in these countries and, hence, their priorities when planning national mitigation policies.

Meanwhile, when the global  $\text{CO}_2$  concentration is cut by half from its peak value, fire emissions could dramatically decrease in some countries (Fig. 4b). This includes mainly countries in the American continent, as well as Indonesia and Russia. The large magnitude of

$\Delta C_{\text{Fire}}$  ( $-1.35 \text{ PgC year}^{-1}$  for the sum of the 10 countries shown in Fig. 4b and  $-1.44 \text{ PgC year}^{-1}$  when aggregated for all available countries) indicates the global-scale co-benefit effect that further accelerates the decrease in atmospheric  $\text{CO}_2$  levels. In other words, if global efforts to reduce carbon emissions and suppress fires in these key regions are successfully implemented, the effectiveness of mitigation policies can be maximized.

Finally, we present an estimation of  $C_{\text{Fire}}$ -adjusted forcing (Fig. 2a). The considerable gap between the forcings with and without  $C_{\text{Fire}}$  adjustment provides significant implications. First, including the climate–fire–carbon cycle feedback, which is currently lacking in most climate models, could lead to substantially diverging climate projections from the true picture. The widely acknowledged scenario-based climate projections (e.g., IPCC reports) may have underestimated the degree of future warming, as the  $C_{\text{Fire}}$  adjustment has not been considered in their driving scenarios. Our results, for which  $C_{\text{Fire}}$  was diagnosed offline, suggest fire-emitted  $\text{CO}_2$  could augment the forcing by  $-2.9\%$  in 2100 and  $4.4\%$  in 2140. It could be even higher if the real-time climate response to  $\text{CO}_2$  comes into play. Second, fire emissions will require stronger mitigation policies than expected to achieve the target emission pathways for  $1.5\text{--}2^\circ\text{C}$  warming, as it can cancel out some mitigation efforts (e.g., ref. 52.). However, although prevailing fire-favorable conditions seem unavoidable under global warming, they may not necessarily lead to actual fire occurrences. Fire control efforts have been constantly ongoing and evaluated as efficient in case studies<sup>53</sup>. Therefore, fire management could be a robust and reliable mitigation action to prevent substantial carbon emissions.

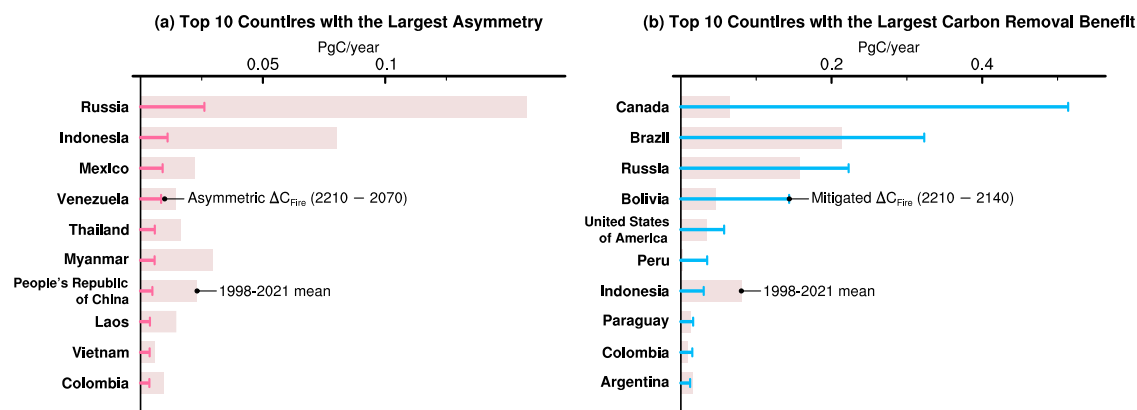


**Fig. 4 | Simulated changes in fire emissions for selected countries. a** Top 10 countries with the largest positive  $\Delta C_{\text{Fire}}$  under symmetric  $\text{CO}_2$  recovery (the asymmetric effect; 2210 minus 2070) and **(b)** top 10 countries for the largest negative  $\Delta C_{\text{Fire}}$  under  $\text{CO}_2$  removal by half from its maximum level (the mitigation effect; 2210 minus 2140). An 11-year window that includes preceding/following 5

years was applied to each time slice. The magnitude of  $\Delta C_{\text{Fire}}$  is denoted by horizontal lines and compared with the current annual mean  $C_{\text{Fire}}$  (1998–2021; filled bars). The units are in  $\text{PgC year}^{-1}$ . Note that the scale of the x-axis differs in the left and right panels.

## Methods

### Datasets

The European Center for Medium Range Weather Forecasts Reanalysis 5 (ERA5; 1998–2021)<sup>39</sup> was used for meteorological variables and the Global Fire Emissions Database (GFED; 1998–2021)<sup>34–36</sup> version 4.1s and Global Fire Assimilation System (GFAS; 2003–2021)<sup>37</sup> for the remotely-sensed biomass burning emission inventory. The carbon emissions are derived based on the burnt area for GFED and fire radiative power (FRP) for GFAS. All data were interpolated to have the same horizontal resolution as CESM ( $288 \times 192$  grids, see below) to facilitate the application of the observed relationship to the model result. When establishing the relationship between the fire weather index (FWI) and carbon emissions ( $C_{\text{Fire}}$ ), ERA5 and GFED were used to ensure the longest available period (1998–2021). The overlapping period for the two is 1997–2021. However, FWI for the first year (1997) was regarded as spin-up and discarded, leaving the actual period of the analysis 1998–2021. We used GFAS C emission data (which is available for a shorter period of 2003–2021) as an auxiliary in the validation of our  $C_{\text{Fire}}$  reconstruction from FWI (Fig. 1a).

### Fire season

Fire season was defined at each grid point based on the climatological annual cycle of GFED  $C_{\text{Fire}}$ : the three months that include the month of the largest mean  $C_{\text{Fire}}$  and its preceding/following months (Supplementary Fig. 6). This definition does not consider the multimodality of fire activity in some regions (e.g., Great Plains<sup>54</sup>), potentially leading to an underestimation of the C emissions. However, in most global fire-prone grids, our definition accounts for more than 60% of the annual total fire activity (Supplementary Fig. 7). Furthermore, comparing the globally aggregated C emission for fire season to the annual total, the selected months capture the annual peak of fire activity well (see text).

### Fire weather index

We used the pyfwi package (<https://github.com/buckinha/pyfwi>, last access: 10 November 2022) to calculate FWI. The required inputs are: local noon-time measurements of 2-m temperature, 2-m RH, 10-m wind speed, and 24-h accumulated precipitation<sup>38</sup>. For the ERA5 reanalysis, 2-m temperature was directly provided from the archive, while the latter three had to be derived. RH was derived from temperature and dew point temperature, wind speed from  $u$  and  $v$  wind components, and 24-h precipitation from hourly precipitation data. In the case of climate model results, the output variables do not meet the exact specification, requiring compromise with available variables. For example, daily maximum of near-surface temperature ('TREFHTMX')

was used instead of the noon temperature. Daily mean values were used for wind speed ('WSPDSRFV'). RH was calculated using daily means of surface pressure, bottom-layer mixing ratio ('QBOT'), and near-surface temperature ('TREF'), where the surface pressure was derived from sea level pressure ('PSL'). Finally, we converted precipitation ('PRECT') into  $\text{mm day}^{-1}$ , which is originally given in  $\text{m s}^{-1}$ .

The above meteorological variables were fed into the package, where FWI is calculated over three stages. At the first stage, fuel moisture over layers is computed in three different fuel moisture codes: the fine fuel moisture code (FFMC), duff moisture code (DMC), and drought code (DC). The results are handed over to the next step, where fire behavior is assessed as the build-up index (BUI) and the initial spread index (ISI). Finally, BUI and ISI are combined to obtain FWI. FWI is unitless and positive, with larger values indicating higher fire danger. The spatial distribution of the observed (ERA5) FWI, simulated (CESM PD) FWI, and their differences are shown in Supplementary Fig. 2 for fire seasons. The simulated FWI exhibits a different extent of bias depending on the region, with a global mean of  $-0.44$  (corresponding to 2.6% of the ERA5 global mean). Therefore, we use the delta change approach to account for this systematic bias—that is, only changes ( $\Delta$ ) relative to the unperturbed state are considered from the simulated result, and the estimation of future  $C_{\text{Fire}}$  is done by adding the simulated  $\Delta C_{\text{Fire}}$  to the current values derived from satellite products.

This approach, assessing potential  $\Delta C_{\text{Fire}}$  based solely on changes in fire weather, does not consider changes in other factors like vegetation, ignition, or human activity, which could affect the future climate–fire emission relationship. While this is intentional (as our primary goal is to isolate and understand the fundamental impact of climatic inertia on fire emissions), it is noteworthy to mention that the performance of our method to capture the interannual variability of  $C_{\text{Fire}}$  is comparable to that of dynamic global vegetation models (DGVMs), which explicitly resolve fire activity and its influencing factors, such as fuel, ignition, and spread. DGVMs yielded temporal correlations with the observed fire emissions (GFED4s, 1997–2012) ranging from  $-0.18$  to  $0.79$ <sup>55</sup>. By comparison, our FWI-based method showed a correlation of  $0.69$  ( $p < 0.05$ ) for the overlapping period (GFED4.1s, 1998–2015), demonstrating its effectiveness in capturing variabilities in fire emissions.

### Preprocessings before regression

A grid point is considered fire-prone if the grid has experienced at least one fire during the GFED observational period (1998–2021). In previous studies (e.g., refs. 20,23.), burnable grids have been determined

depending on the land cover type—i.e., whether there is burnable biomass or not. Our definition produces a mask similar to theirs, with the incombustible areas covered mainly by desert and ice.

Unlike meteorological variables that bear continuity with adjacent grid points, the observed fire variables (e.g., burnt area, C emission, etc.) are highly localized. However, pinpointing the exact location of future fire emissions is improbable given that ignition sources tend to be probabilistic and stochastic, and is out of the purpose of this study. Therefore, we applied the moving average in the horizontal dimension on the  $C_{\text{Fire}}$  data to ease its locality, as well as on FWI to ensure that the two variables are representative of the same area (i.e., to maintain the physical consistency). We used a  $5 \times 7$  (lon  $\times$  lat) grid box as the moving window, which corresponds to a spatial scale of  $\sim 5^\circ \times 5.6^\circ$ . Similar approaches have been used in previous studies<sup>22,40</sup>.

To rule out the anthropogenically driven trend in FWI and focus on the year-to-year relationship between FWI and  $C_{\text{Fire}}$ , linear detrending was applied to FWI; but not to C emissions. This is because a few extreme events can drive trends in  $C_{\text{Fire}}$ , which can be portrayed by a lack of linearity (i.e.,  $R^2$  of regression onto time) in their time series (Supplementary Fig. 8). In this situation, removing linear trends may substantially distort the data property, for example, yielding negative values of C emissions which are unrealistic. Although some regions, such as the south of the Sahara, exhibit relatively strong linearity, removing their trends does not significantly affect our FWI- $C_{\text{Fire}}$  regression model (Fig. 1b), as the difference of regression coefficients with and without detrending is less than an order of  $10^{-5}$ .

### CESM experiments

The Community Earth System Model (CESM)<sup>45</sup> version 1.2 was used to simulate the global climate response under a CO<sub>2</sub> removal scenario. In CESM, the atmosphere (The Community Atmospheric Model version 5, CAM5), ocean (The Parallel Ocean Program version 2, POP2), sea ice (The Community Ice Code version 4, CICE4), and land (Community Land Model version 4, CLM4) models are tied to a central coupler. The horizontal resolution for CAM5 and CLM4 was  $1^\circ$ , and CAM5 had 30 vertical layers. For POP2 and CICE4, the longitudinal resolution was  $1^\circ$  while the latitudinal resolution varied from  $1/3^\circ$  near the equator to  $1/2^\circ$  near the poles. The vertical resolution of POP2 was 60 levels.

The model was subjected to an idealized CO<sub>2</sub> forcing: Starting from the present-day (PD; year 2000) level of 367 ppm, it was ramped up at a rate of 1% per year until it reached 4 times its initial value (1468 ppm), and then ramped down symmetrically. This pathway is analogous to the ‘CDRMIP-reversibility’ protocol in Coupled Model Intercomparison Project Phase 6 (CMIP6), except that CDRMIP-reversibility employed the preindustrial level (284 ppm) as the initial value of CO<sub>2</sub><sup>56</sup>. Although quadrupling itself may not be feasible given fossil fuel constraints<sup>57</sup>, such an idealized approach benefits us in improving a fundamental understanding of the climate system. In addition, the rate of increase,  $1\% \text{ year}^{-1}$ , is comparable to the ‘high emission’ scenarios such as the Representative Concentration Pathway (RCP) 8.5 (arguably, the ‘business-as-usual’<sup>58,59</sup>) and SSP5-8.5 used in Intergovernmental Panel on Climate Change (IPCC) reports. The rapid decrease after the peak is assumed to be driven by anthropogenic efforts to achieve negative emissions, going beyond net-zero. Under the given scenario, it takes 140 model years for the forcing to peak (year 2140), and it hits doubled CO<sub>2</sub> twice in 2070, and 2210, respectively. Once the forcing returns to its initial value (367 ppm) in 2280, it is maintained constant. 28 ensemble simulations were performed with different initial conditions, which branched out from the baseline (PD) experiment of 900 years. For the baseline run, no ensemble simulation was conducted, and the last 100 years were analyzed in this study.

### Multiple regression analysis

Multiple regression allows identification of the predictand’s sensitivity to each predictor variable. Here, the predictand is FWI, and the

predictors are  $T$ , precipitation (Pr), wind speed (WS), and RH. The equation can be written as

$$\Delta \text{FWI} = \gamma_T \Delta T + \gamma_{\text{Pr}} \Delta \text{Pr} + \gamma_{\text{WS}} \Delta \text{WS} + \gamma_{\text{RH}} \Delta \text{RH} + \varepsilon \quad (1)$$

where the parameter  $\gamma_i$  denotes the sensitivity of FWI to the  $i$ -th variable, and  $\varepsilon$  is residual. Each physical variable ( $\Delta \text{FWI}$ ,  $\Delta T$ ,  $\Delta \text{Pr}$ ,  $\Delta \text{WS}$ , and  $\Delta \text{RH}$ ) is obtained at each grid point as the difference between 2070 and 2210 from 28 ensemble simulations. For a direct comparison of  $\gamma$  for variables with different units, the input weather variables were standardized. This way, all parameters are obtained non-dimensional, and the results are compared in Supplementary Fig. 5. In most areas, the highest sensitivity (in magnitude) is seen for RH among the four variables, indicating that even a small decrease in RH could lead to a sharp increase in FWI. However, the final contribution to FWI is determined by not only the sensitivity ( $\gamma_i$ ) but also the magnitude of change ( $\Delta_i$ ). It can be evaluated as a combination of the two,  $\gamma_i \times \Delta_i$ , and the resulting spatial patterns for each variable are shown in Supplementary Fig. 4. Also shown in Supplementary Fig. 4 are the reconstructed ( $\sum_i \gamma_i \times \Delta_i$ ,  $i = T, \text{Pr}, \text{WS}, \text{and RH}$ ) and the simulated  $\Delta \text{FWI}$ . Globally averaged results for each weather variable are shown in Fig. 3a with the 95% bootstrap interval ( $N = 1000$ ).

### Decomposition of $\Delta \text{RH}$

RH is defined as the ratio of the amount of moisture in the air ( $e$ , in Pa) to the maximum capacity that the air can hold [ $e_s(T)$ , in Pa], where  $e_s(T)$  is determined by the air temperature<sup>60,61</sup>:

$$\text{RH} = \frac{e}{e_s(T)} \quad (2)$$

$$e_s(T) = 611.21 \times \exp\left(\frac{17.62 \times T}{T + 243.12}\right) \quad (3)$$

By considering a situation where the air temperature is perturbed by  $\Delta T$ , changes in RH solely due to temperature ( $\Delta \text{RH}_T$ ) can be obtained as follows.

$$\begin{aligned} \Delta \text{RH}_T &= \frac{e}{e_s(T + \Delta T)} - \frac{e}{e_s(T)} \\ &= e \left\{ \frac{e_s(T) - e_s(T + \Delta T)}{e_s(T + \Delta T) \cdot e_s(T)} \right\} \\ &= -\text{RH} \left\{ \frac{e_s(T + \Delta T) - e_s(T)}{e_s(T + \Delta T)} \right\} \\ &= -\text{RH} \left\{ \frac{\Delta e_s}{e_s(T + \Delta T)} \right\} \end{aligned} \quad (4)$$

The difference in saturation vapor pressure between initial and final states was denoted by  $\Delta e_s$ . The negative sign in the final form indicates that RH is lowered (negative  $\Delta \text{RH}_T$ ) when the saturation vapor pressure is raised by warming (positive  $\Delta e_s$ ) and vice versa.

In CESM results,  $\Delta \text{RH}_T$  for 2210–2070 is evaluated by feeding model-simulated RH (2070),  $T$  (2070), and  $T + \Delta T$  (2210) into Eq. (4), with substituting Eq. (3) for  $e_s$ . The difference between  $\Delta \text{RH}_T$  and the total RH change ( $\Delta \text{RH}$ , directly obtained from the model output) can be regarded to have been induced by moisture loss/supply.

### Data availability

The GFED data can be downloaded from [https://daac.ornl.gov/cgi-bin/dsviewer.pl?ds\\_id=1293](https://daac.ornl.gov/cgi-bin/dsviewer.pl?ds_id=1293), GFAS emissions from <https://ads.atmosphere.copernicus.eu/cdsapp#!/dataset/cams-global-fire-emissions-gfas?tab=form>, ERA5 datasets from the European Center for Medium-Range Weather Forecasts (<https://climate.copernicus.eu/climate-reanalysis>), and CDRMIP results from the Earth System Grid Federation (ESGF) node (<https://esgf.nci.org.au/projects/cmip6-nci/>). The pyfwi code



(<https://code.google.com/archive/p/pyfwi/>) was used for the FWI calculation. The code of CESM1 is available from <http://www.cesm.ucar.edu/models>. The data used in this study have been deposited in figshare<sup>62</sup> (<https://figshare.com/s/3d5f63fcd74743c54356?file=48551125>, <https://doi.org/10.6084/m9.figshare.25000925.v1>) except for the raw outputs of CESM simulations which are available from the corresponding author upon request due to their large size.

## Code availability

The codes used for data processing are available at ref. 62 and also at Code Ocean (<https://doi.org/10.24433/CO.8021617.v1>).

## References

- Masoudvaziri, N., Ganguly, P., Mukherjee, S. & Sun, K. Integrated risk-informed decision framework to minimize wildfire-induced power outage risks: A county-level spatiotemporal analysis. *30th Eur. Saf. Reliab. Conf. ESREL 2020 15th Probabilistic Saf. Assess. Manag. Conf. PSAM 2020* 4493–4500 (2020).
- Hope, E. S., McKenney, D. W., Pedlar, J. H., Stocks, B. J. & Gauthier, S. Wildfire suppression costs for Canada under a changing climate. *PLoS One* **11**, 1–18 (2016).
- González-Cabán, A. The economic dimension of wildland fires. *Vegetation Fires and Global Change – Challenges for Concerted International Action. A white paper directed to the United Nations and international organizations* 229–237 at <http://treeseearch.fs.fed.us/pubs/44383> (2013).
- PREVAIL (Prevention Action Increases Large Fire Response Preparedness). WP2-Deliverable 2.3 Report on wildfire suppression cost analysis. (2020).
- Agne, M. C., Fontaine, J. B., Enright, N. J. & Harvey, B. J. Fire interval and post-fire climate effects on serotinous forest resilience. *Fire Ecol.* **18**, 22 (2022).
- Parashar, A. & Biswas, S. The impact of forest fire on forest biodiversity in the Indian Himalayas (Uttaranchal). in *XII World Forestry Congress*. Vol. 358 (2003).
- Swetnam, W. Fire history and climate change in giant sequoia groves author (s): Thomas W. Swetnam Published by: American Association for the Advancement of Science Stable URL: <http://www.jstor.org/stable/2882622>. **262**, 885–889 (1993).
- de Barros, A. E. et al. Wildfires disproportionately affected jaguars in the Pantanal. *Commun. Biol.* **5**, 1–12 (2022).
- Solomon, S. et al. Chlorine activation and enhanced ozone depletion induced by wildfire aerosol. *Nature* **615**, 259–264 (2023).
- Garcês, A. & Pires, I. The hell of wildfires: the impact on wildlife and its conservation and the role of the veterinarian. *Conservation* **3**, 96–108 (2023).
- Seidl, R. et al. Forest disturbances under climate change. *Nat. Clim. Chang.* **7**, 395–402 (2017).
- Bowman, D. M. J. S. et al. Fire in the Earth system. *Sci.* **324**, 481–484 (2009).
- Harrison, S. P. et al. The biomass burning contribution to climate-carbon-cycle feedback. *Earth Syst. Dyn.* **9**, 663–677 (2018).
- Jacobson, A. R. et al. CarbonTracker CT2022. **1** <https://doi.org/10.25925/z1gj-3254> (2023).
- Dennison, P. E., Brewer, S. C., Arnold, J. D. & Moritz, M. A. Large wildfire trends in the western United States, 1984–2011. *Geophys. Res. Lett.* **41**, 2928–2933 (2014).
- Ponomarev, E. I., Kharuk, V. I. & Ranson, K. J. Wildfires dynamics in Siberian larch forests. *Forests* **7**, (2016).
- Jolly, W. M. et al. Climate-induced variations in global wildfire danger from 1979 to 2013. *Nat. Commun.* **6**, 1–11 (2015).
- Jones, M. W. et al. Global and regional trends and drivers of fire under climate change. *Rev. Geophys.* **60**, 1–76 (2022).
- Williams, A. P. et al. Observed impacts of anthropogenic climate change on wildfire in California. *Earth's Futur.* **7**, 892–910 (2019).
- Jain, P., Castellanos-Acuna, D., Coogan, S. C. P., Abatzoglou, J. T. & Flannigan, M. D. Observed increases in extreme fire weather driven by atmospheric humidity and temperature. *Nat. Clim. Chang.* **12**, 63–70 (2022).
- Richardson, D. et al. Global increase in wildfire potential from compound fire weather and drought. *npj. Clim. Atmos. Sci.* **5**, (2022).
- Bedia, J. et al. Global patterns in the sensitivity of burned area to fire-weather: implications for climate change. *Agric. Meteorol.* **214**, 369–379 (2015).
- Abatzoglou, J. T., Williams, A. P. & Barbero, R. Global emergence of anthropogenic climate change in fire weather indices. *Geophys. Res. Lett.* **46**, 326–336 (2019).
- Dong, C. et al. The season for large fires in Southern California is projected to lengthen in a changing climate. *Commun. Earth Environ.* **3**, 0–2 (2022).
- Bowman, D. M. J. S. et al. Human exposure and sensitivity to globally extreme wildfire events. *Nat. Ecol. Evol.* **1**, 58 (2017).
- Pimont, F. et al. Future expansion, seasonal lengthening and intensification of fire activity under climate change in southeastern France. *Int. J. Wildl. Fire* **32**, 4–14 (2022).
- Son, R. et al. Changes in fire weather climatology under 1.5 °C and 2.0 °C warming. *Environ. Res. Lett.* **16**, 034058 (2021).
- Yu, Y. et al. Machine learning-based observation-constrained projections reveal elevated global socioeconomic risks from wildfire. *Nat. Commun.* **13**, (2022).
- Ward, D. S. et al. The changing radiative forcing of fires: global model estimates for past, present and future. *Atmos. Chem. Phys.* **12**, 10857–10886 (2012).
- Kim, S.-K. et al. Widespread irreversible changes in surface temperature and precipitation in response to CO<sub>2</sub> forcing. *Nat. Clim. Chang.* **12**, 834–840 (2022).
- Kug, J. S. et al. Hysteresis of the intertropical convergence zone to CO<sub>2</sub> forcing. *Nat. Clim. Change* vol. **12**, 47–53 (2022).
- An, S.-I. et al. Global cooling hiatus driven by an AMOC overshoot in a carbon dioxide removal scenario. *Earth's Futur.* **9**, (2021).
- Oh, H. et al. Contrasting hysteresis behaviors of northern hemisphere land monsoon precipitation to CO<sub>2</sub> pathways. *Earth's Futur.* **10**, e2021EF002623 (2022).
- Giglio, L., Randerson, J. T. & Van Der Werf, G. R. Analysis of daily monthly and annual burned area using the fourth-generation global fire emissions database (GFED4). *J. Geophys. Res.* **118**, 317–328 (2013).
- Randerson, J. T., van der Werf, G. R., Giglio, L., Collatz, G. J. & Kasibhatla, P. S. Global fire emissions database, (GFEDv4). at <https://doi.org/10.3334/ORNLDAAAC/1293> (2017).
- Van Der Werf, G. R. et al. Global fire emissions estimates during 1997–2016. *Earth Syst. Sci. Data* . **9**, 697–720 (2017).
- Kaiser, J. W. et al. Biomass burning emissions estimated with a global fire assimilation system based on observed fire radiative power. *Biogeosciences* **9**, 527–554 (2012).
- Van Wagner, C. E. *Development And Structure Of The Canadian Forest Fire Weather Index System*. Forestry (1987).
- Hersbach, H. et al. ERA5 hourly data on single levels from 1940 to present. at <https://doi.org/10.24381/cds.adbb2d47> (2023).
- Di Giuseppe, F. et al. The potential predictability of fire danger provided by numerical weather prediction. *J. Appl. Meteorol. Climatol.* **55**, 2469–2491 (2016).
- Abatzoglou, J. T., Williams, A. P., Boschetti, L., Zubkova, M. & Kol-den, C. A. Global patterns of interannual climate–fire relationships. *Glob. Chang. Biol.* **24**, 5164–5175 (2018).
- Pausas, J. G. & Ribeiro, E. The global fire-productivity relationship. *Geob. Ecol. Biogeogr.* **22**, 728–736 (2013).
- Yu, Z., Loisel, J., Brosseau, D. P., Beilman, D. W. & Hunt, S. J. Global peatland dynamics since the last glacial maximum. *Geophys. Res. Lett.* **37**, L13402 (2010).



44. Zheng, B. et al. Record-high CO<sub>2</sub> emissions from boreal fires in 2021. *Science*. **379**, 912–917 (2023).
45. Hurrell, J. W. et al. The community earth system model: a framework for collaborative research. *Bull. Am. Meteorol. Soc.* **94**, 1339–1360 (2013).
46. Maraun, D. & Widmann, M. *Statistical Downscaling and Bias Correction for Climate Research*. (Cambridge University Press, 2018).
47. Pechony, O. & Shindell, D. T. Driving forces of global wildfires over the past millennium and the forthcoming century. *Proc. Natl Acad. Sci. USA*. **107**, 19167–19170 (2010).
48. Kim, J. S., Kug, J. S. & Jeong, S. J. Intensification of terrestrial carbon cycle related to El Niño-southern oscillation under greenhouse warming. *Nat. Commun.* **8**, 1–8 (2017).
49. Sherwood, S. & Fu, Q. A drier future? *Sci.* **343**, 737–739 (2014).
50. Park, S. W. & Kug, J. S. A decline in atmospheric CO<sub>2</sub> levels under negative emissions may enhance carbon retention in the terrestrial biosphere. *Commun. Earth Environ.* **3**, 2–9 (2022).
51. Meinshausen, M. et al. The shared socio-economic pathway (SSP) greenhouse gas concentrations and their extensions to 2500. *Geosci. Model Dev.* **13**, 3571–3605 (2020).
52. Jerrett, M., Jina, A. S. & Marlier, M. E. Up in smoke; California's greenhouse gas reductions could be wiped out by 2020 wildfires. *Environ. Pollut.* **310**, (2022).
53. Plucinski, M. P. Contain and control: Wildfire suppression effectiveness at incidents and across landscapes. *Curr. Rep.* **5**, 20–40 (2019).
54. Balik, J. A. et al. Biogeographic patterns of daily wildfire spread and extremes across North America. *Front. Glob. Chang.* **7**, 1–14 (2024).
55. Li, F. et al. Historical (1700–2012) global multi-model estimates of the fire emissions from the fire modeling intercomparison project (FireMIP). *Atmos. Chem. Phys.* **19**, 12545–12567 (2019).
56. Keller, D. P. et al. The Carbon Dioxide Removal Model Inter-comparison Project (CDRMIP): Rationale and experimental protocol for CMIP6. *Geosci. Model Dev.* **11**, 1133–1160 (2018).
57. Wang, J., Feng, L., Tang, X., Bentley, Y. & Höök, M. The implications of fossil fuel supply constraints on climate change projections: A supply-side analysis. *Futures* **86**, 58–72 (2017).
58. Schwalm, C. R., Glendon, S. & Duffy, P. B. RCP8.5 tracks cumulative CO<sub>2</sub> emissions. *Proc. Natl Acad. Sci. USA*. **117**, 19656–19657 (2020).
59. Hausfather, Z. & Peters, G. P. Emissions - the 'business as usual' story is misleading. *Nature* **577**, 618–620 (2020).
60. Huang, X., Abolt, C. J. & Bennett, K. E. Brief communication: effects of different saturation vapor pressure calculations on simulated surface-subsurface hydrothermal regimes at a permafrost field site. 1–15 (2023).
61. Alduchov, O. A. & Eskridge, R. E. Improved Magnus form approximation of saturation vapor pressure. *J. Appl. Meteorol.* **35**, 601–609 (1996).
62. Kim, H.-J. Dataset 'Pervasive fire danger. continued a Negat. Emiss. scenario'. <https://doi.org/10.6084/m9.figshare.25000925> (2024).

## Acknowledgements

This work was supported by National Research Foundation of Korea (NRF) grants funded by the Korean government (MSIT) (NRF-2018R1A5A1024958 to S.-I.A., NRF-2022M3I6A1085990 to H.-J.K., NRF-2022R1A3B1077622 to J.-S. Kug and J.-H.O.) by Korea Environmental Industry & Technology Institute (KEITI) through 'Project for developing an observation-based GHG emissions geospatial information map',

funded by Korea Ministry of Environment (MOE) (RS-2023-00232066 to J.-S. Kim), by CityU Start-up Grant for New Faculty (Project No. 9610581 to J.-S. Kim), and by Center for Ocean Research in Hong Kong and Macao (CORE), which is a joint research center for ocean research between Laoshan Laboratory and HKUST (to H.-J.K. and J.-S. Kim). The CESM simulation was conducted on the supercomputer supported by the National Center for Meteorological Supercomputer of Korea Meteorological Administration (KMA), the National Supercomputing center with supercomputing resources, associated technical support (KSC-2021-CHA-0030), and the Korea Research Environment Open Network (KREONET).

## Author contributions

J.-S. Kim and H.-J.K. conceived the idea of this work and conducted the investigation. S.-I.A., J.-S. Kug, and J.S. developed and executed the CESM model simulation. J.-H.O. and J.S. participated in the scientific discussion. Methodologies for data analysis were designed by H.-J.K., J.-S. Kim, and S.-I.A. All authors contributed to the interpretation of the results and editing of the manuscript.

## Competing interests

The authors declare no competing interests.

## Additional information

**Supplementary information** The online version contains supplementary material available at <https://doi.org/10.1038/s41467-024-54339-2>.

**Correspondence** and requests for materials should be addressed to Jin-Soo Kim or Soon-Il An.

**Peer review information** *Nature Communications* thanks Yue Li and Yan Yu for their contribution to the peer review of this work. A peer review file is available.

**Reprints and permissions information** is available at <http://www.nature.com/reprints>

**Publisher's note** Springer Nature remains neutral with regard to jurisdictional claims in published maps and institutional affiliations.

**Open Access** This article is licensed under a Creative Commons Attribution-NonCommercial-NoDerivatives 4.0 International License, which permits any non-commercial use, sharing, distribution and reproduction in any medium or format, as long as you give appropriate credit to the original author(s) and the source, provide a link to the Creative Commons licence, and indicate if you modified the licensed material. You do not have permission under this licence to share adapted material derived from this article or parts of it. The images or other third party material in this article are included in the article's Creative Commons licence, unless indicated otherwise in a credit line to the material. If material is not included in the article's Creative Commons licence and your intended use is not permitted by statutory regulation or exceeds the permitted use, you will need to obtain permission directly from the copyright holder. To view a copy of this licence, visit <http://creativecommons.org/licenses/by-nc-nd/4.0/>.

© The Author(s) 2024, corrected publication 2025